ADVANCED FUNCTIONAL MATERIALS
www.afm-journal.de

# Harnessing Non-Covalent Protein–Protein Interaction Domains for Production of Biocatalytic Materials Systems

*Julian S. Hertel, Maria Alessandra Martini, Marius Stoeckle, Annika J. Weber, Kersten S. Rabe, and Christof M. Niemeyer**

**Industrial biocatalysis has the potential to enable sustainable and environmentally friendly processes in the chemical industry. In continuous production systems, immobilized enzymes are required as catalysts, and providing them in a carrier-free form is preferable to maximize effective reactor space usage. This study explores the use of non-covalent protein interaction domains for fabricating catalytically active all-enzyme hydrogel (AEH) materials. For this, enzymes of a binary interacting cascade – an alcohol dehydrogenase and a glucose-1-dehydrogenase for cofactor regeneration – are genetically fused to various non-covalent binding motifs (PDZ, GBD, SH3), enabling self-assembly into non-covalent AEHs. The resulting materials are generated both in living E. coli cells and from purified enzymes as monodisperse enzyme foams. While in-cell AEHs show no significant advantages over non-assembled cascades in continuous flow reactors, the AEH foams demonstrated excellent performance. Optimized systems based on SH3 and PDZ domains, despite a 100-fold difference in binding affinity, achieved stable conversions above 70% over 30 h. Notably, drying the enzyme foams significantly improved both mechanical stability and catalytic activity. The successful application of this approach to a different enzyme system based on phenolic acid decarboxylase further underscores its versatility and suitability for developing robust biocatalytic materials for sustainable industrial processes.**

## 1. Introduction

Industrial biocatalysis is widely regarded as a transformative approach for the development of a sustainable economy.[1,2] The validated advantages of biocatalytic processes, coupled with the broad spectrum of available enzymes, enable the "green" production of value-added molecules, including the stereoselective production of high-priced pharmaceutical ingredients.[3] To advance the field, key challenges such as the development of enzyme cascades, standardization of production processes, and implementation of continuous process technology must be addressed and, therefore, flow biocatalysis has gathered significant attention.[4] This technology leverages the principles of established flow chemistry, which employs continuous, compartmentalized, and machine-assisted modular chemical synthesis, to address the unique demands of biocatalytic processes. The respective developments include facilitating the gentle immobilization of substantial quantities of enzyme biocatalysts within micro-structured flow reactors.[5] Inspired by nature's principle of spatially arranged biomolecules, strategies such as enzyme organization and protein fusions enhance multienzyme biocatalysis by improving product formation and intermediate depletion while minimizing competing reactions. However, challenges like uncontrolled enzyme aggregation and reduced catalytic activity highlight the need for advanced materials development.[6]

To address these challenges, we developed a site-specific SpyCatcher/SpyTag[7] (SC/ST)-based covalent conjugation method to create advanced self-assembling all-enzyme hydrogels (AEH).[8] These materials form stable isopeptide bonds under physiological conditions, offer precise stoichiometric control of interacting enzymes, and have been successfully applied to various systems, enabling durable microfluidic reactors,[9–11] as well as inCell AEH production using polycistronic vectors in *E. coli*.[12] Furthermore, monodisperse foam formulations enhance AEH by combining high enzyme concentration and solid anchorage, while still ensuring efficient mass transport, providing a robust solution for flow biocatalysis.[13] Previous AEH materials have all been produced through stable covalent linkage mediated through the SC/ST system, however, non-covalent protein assemblies could offer advantages due to their dynamic and reversible nature. They inherently allow for adaptable aggregation/disaggregation and a lower risk of permanent structural damage, while still enabling functional

J. S. Hertel, M. A. Martini, M. Stoeckle, A. J. Weber, K. S. Rabe, C. M. Niemeyer
Institute for Biological Interfaces (IBG1)
Karlsruhe Institute of Technology (KIT)
Hermann-von-Helmholtz-Platz 1, D-76344 Eggenstein-Leopoldshafen, Germany
E-mail: niemeyer@kit.edu

The ORCID identification number(s) for the author(s) of this article can be found under https://doi.org/10.1002/adfm.202513931



**DOI: 10.1002/adfm.202513931**

organization and activity. In nature a multitude of non-covalent protein-protein interaction domains like PDZ (named after the first three proteins found to contain this domain (PSD-95, Dlg, ZO-1)), GBD (GTPase-Binding-Domain) or SH3 (Src Homology 3)[14] orchestrate the assembly of functional complexes for signal transduction and metabolism in cells.[15] While several approaches have utilized protein-protein interaction domains for in vivo studies with metabolically engineered microbial cells,[14,16] the application of this strategy to biocatalytic materials systems has been largely unexplored.[17] It was particularly unclear whether these non-covalent binding systems could facilitate the assembly of AEH and, if so, whether the non-covalently linked AEHs (ncAEHs) would exhibit comparable material properties in terms of catalytic activity and mechanical resilience. This is especially relevant to the recently observed phenomenon where foams derived from covalent AEHs gained mechanical stability over time through aging achieved by drying at moderate temperatures.[13]

To address these questions, this study investigates the use of non-covalent interaction domains for the production of biocatalytic AEH materials. For this purpose, the binary interacting enzyme system of LbADH (alcohol dehydrogenase from *Lactobacillus brevis*) and BsGDH (glucose-1-dehydrogenase from *Bacillus subtilis*) was employed to catalyze the two-step *(R)*-selective reduction of 5-nitrononane-2,8-dione (NDK **1**) to hydroxyketones **2** and diol **3** (**Figure** 1A). The enzymes were genetically modified with different non-covalent binding motifs (PDZ, GBD, SH3, see Figure 1B), enabling the formation of ncAEH both in living *E. coli* cells (inCell-ncAEH) and as monodisperse enzyme foams (ncAEH foams) (Figure 1C). We found that the inCell-ncAEH showed no substantial improvement in catalytic activity compared to isolated enzymes, however, ncAEH foams demonstrated remarkable biocatalytic activity and mechanical resilience under flow conditions.

## 2. Results and Discussion

### 2.1. Physicochemical Characterization of Non-Covalent Interaction Domains

Based on the established system of the highly (*R*)-selective alcohol dehydrogenase from *Lactobacillus brevis* (LbADH) and the nicotinamide adenine dinucleotide phosphate (NADPH)-regenerating glucose-1-dehydrogenase from *Bacillus subtilis* (BsGDH),[13] a range of genetic fusions with various non-covalent interaction domains was generated.

To systematically investigate the influence of binding strength in non-covalent systems on ncAEH formation, three systems with varying affinities were selected from the literature. The weakest interaction system was the PDZ system (derived from naturally occurring proteins such as PSD-95, Dlg, and ZO-1) with a dissociation constant of $K_d \approx 8.0$ µM).[18,19] In contrast, the SH3 system (based on the Src Homology 3 domain) exhibited the strongest affinity ($K_d \approx 0.1$ µM),[14,19] while the GBD system (derived from the GTPase-binding domain) displayed intermediate affinity ($K_d \approx 1$ µM).[20] All three systems consist of a ligand (L) and a ligand-binding domain (B), which interact through distinct molecular interactions. A detailed overview of these systems is provided in Figure S1 (Supporting Information). In this study, the ligands of the three systems were uniformly fused with the cofactor regeneration enzyme BsGDH, resulting in the enzymes GDH-PDZ$^{L}$, GDH-GBD$^{L}$ and GDH-SH3$^{L}$. Similarly, the ligand-binding domains were uniformly coupled to the stereoselective ketoreductase LbADH, resulting in the enzymes ADH-PDZ$^{B}$, ADH-GBD$^{B}$ and ADH-SH3$^{B}$ (Figure 1B). All fusion enzymes were recombinantly overexpressed in *E. coli* and purified to homogeneity using chromatographic methods (Figure S1, Supporting Information).

We then compared the catalytic activity of the novel fusion proteins to quantitatively assess their performance relative to the previously characterized wild-type enzymes by using the NDK **1** reaction shown in Figure 1A.[8] The results showed that ADH-PDZ$^{B}$ retained the same activity as the wild-type (WT) ADH, whereas ADH-GBD$^{B}$ lost nearly all activity (**Figure** 2A). The fusion of SH3$^{B}$ led to a sharp decline in activity, though it still retained a substantial level of residual activity. In contrast, all GDH variants fused with the small ligand domain (<4 kDa) showed a slight increase in activity, as compared to the native variant. The influence of a genetic fusion on an enzyme's activity is generally challenging to predict and often difficult to rationalize afterwards, as both increases and decreases in activity are observed in practice and can be linked to alterations in protein tertiary structure.[21] To investigate the activity losses associated with GBD$^{B}$ and SH3$^{B}$ fusions, structural predictions were performed using Chai-1 modelling[22] to examine their three-dimensional architecture (Figure S2, Supporting Information). The results indicated that, in contrast to SH3$^{B}$ or PDZ$^{B}$, GBD$^{B}$ is intrinsically unstructured, which may explain the observed loss of activity through improper protein folding or steric hindrance.

The activities of the coupled enzymes were examined by mixing equimolar amounts of the respective ADH and GDH enzyme variants (Figure 2B). The results show that the SC/ST fusion exhibits slightly reduced activity compared to the wild-type enzymes, highlighting the influence of enzyme fusion on performance. Similarly, the comparison of non-covalent fusions in terms of coupled activity mirrors the trends observed with the individual enzymes (Figure 2A). The PDZ variant displayed activity comparable to the wild-type enzymes. In contrast, the reduced activity of ADH-SH3$^{B}$ in the coupled assay was partially mitigated by the high activity of GDH-SH3$^{L}$, resulting in an overall performance similar to that of the covalent SC/ST fusion. As anticipated based on the low activity of the ADH-GBD$^{B}$ component, the GBD system showed minimal activity in the coupled assay. A detailed overview on the kinetic parameters is given in Figures S3 and S4 (Supporting Information).

Next, we investigated whether the non-covalent assembly of the L-B systems leads to formation of self-assembled all enzyme hydrogel (ncAEH) nanogel materials comprised of small nanoscaled particles, similar as observed for the covalent assembly systems.[8] To this end, dynamic light scattering (DLS) was employed to measure changes of the hydrodynamic radius of the purified proteins in the presence of their binding partners (Figure 2C–E). For all enzyme fusions except GDH-GBD$^{L}$, the isolated LbADH (dark blue curves in Figure 2C–E) and BsGDH (turquoise) variants exhibited hydrodynamic diameters of ≈10 nm, indicating their expected behavior of remaining tetrameric without assembling or aggregating in the absence of a complementary binding partner. The unexpected

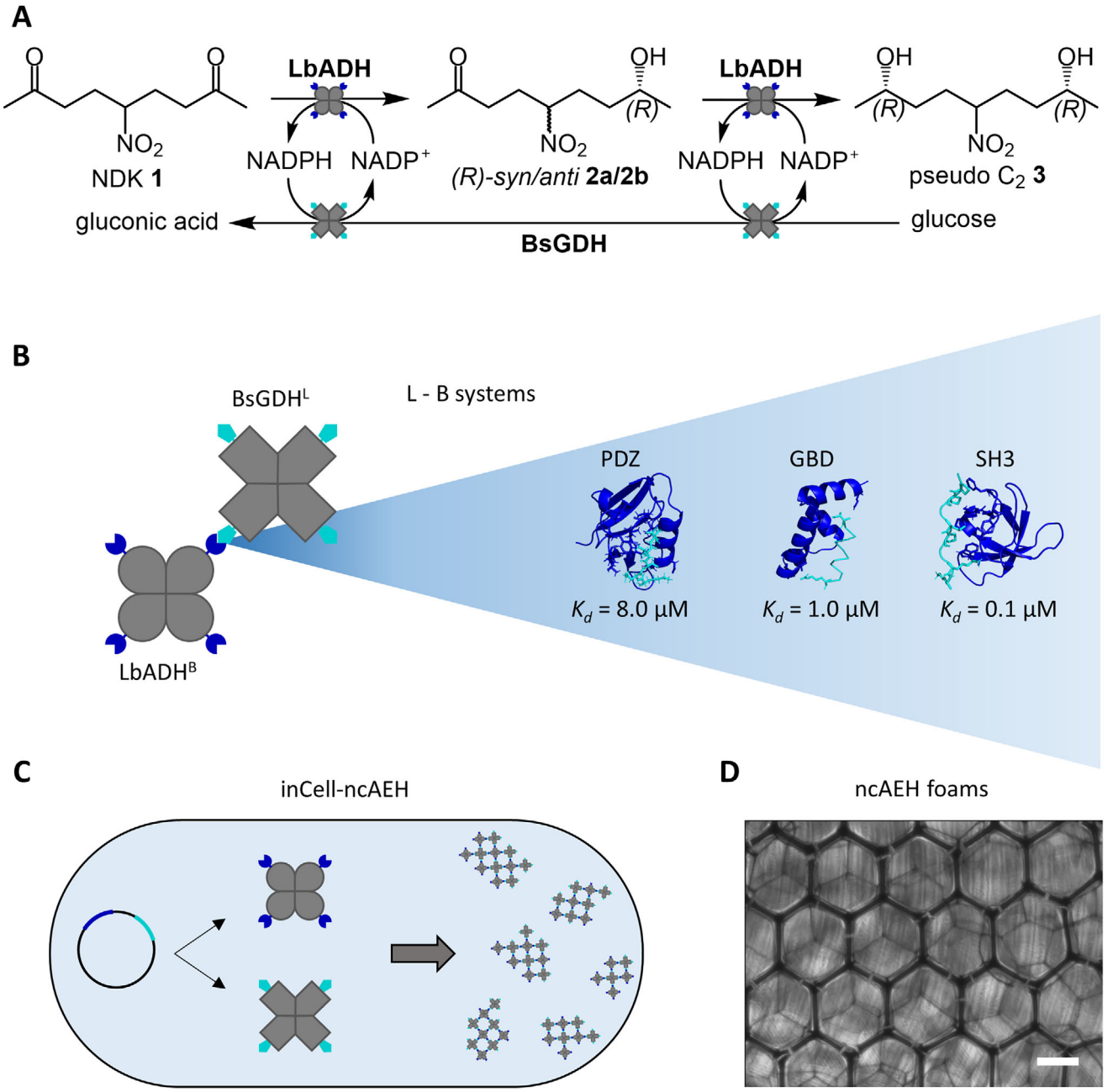


**Figure 1.** A) The enzymes LbADH and BsGDH are used for the two-step (R)-selective reduction of substrate 5-nitrononane-2,8-dione (NDK 1) to the corresponding hydroxyketones 2 and diol 3 products. B) The enzymes are fused to the non-covalent ligand and binding systems (L-B systems) based on either PDZ, GBD or SH3 domains. Literature values of $K_d$ for the isolated systems are shown. The feasibility of forming non-covalent AEH materials was investigated using two different flow biocatalytic setups based on either whole cells (inCell-ncAEH, C) or isolated enzymes formulated as monodisperse foams (ncAEH foams, D) Scale bar: 100 µm. Note that the schematic representation in (C) is a simplified, idealized depiction of the supramolecular protein networks. Although the self-assembly of the soft, flexible protein building blocks does not produce crystalline or amorphous structures, the illustration serves to visually convey the conceptual organization of the networks.

aggregation of GDH-GBD$^L$ (turquoise curve in Figure 2D) remains unclear but may be attributed to the insufficient stability of the protein's tertiary structure during prolonged incubation under the given assay conditions. In contrast, equimolar mixtures of complementary binding partners resulted in a substantial increase in hydrodynamic diameter, indicating the formation of ncAEH nanogel particles. Significant differences were observed in the rate of increase in hydrodynamic diameter. The SH3 system exhibited the fastest and most pronounced nanogel formation (1.97 ± 0.31 Δz-average min$^{-1}$), reaching an average size of 33 nm. This was followed by the PDZ system, which formed particles more slowly (0.12 ± 0.001 Δz-average min$^{-1}$),

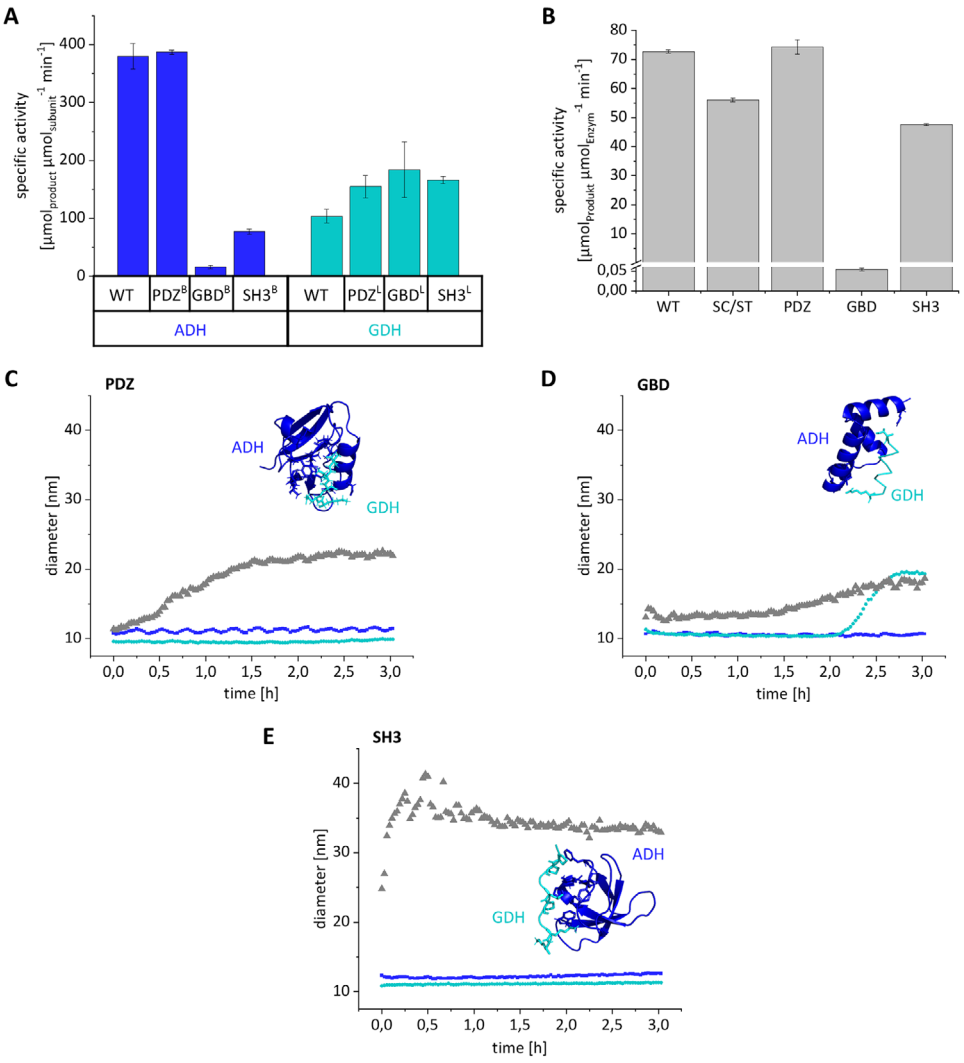


**Figure 2.** A) Comparison of specific activities of ADH-PDZ$^B$, ADH-GBD$^B$ and ADH-SH3$^B$ (dark blue) and GDH-PDZ$^L$, GDH-GBD$^L$ and GDH-SH3$^L$ (turquoise) with their corresponding wild type enzyme. B) Overview of the coupled activities for the systems based on WT, SC/ST, PDZ, GBD, or SH3 enzyme variants. C,D) Time dependent measurement of nanogel formation in solution. For each sample, a total protein concentration of 0.5 mM was used, with measurements of the hydrodynamic diameter (z-average) taken every 100 seconds over a period of 3 h at 25 °C. The equimolar mixture of binding partners is represented by gray curves, while the corresponding individual proteins are shown in dark blue (binding domains) and turquoise (ligands). Sample size (n) in Figures A – D n≥2. All error bars represent the standard deviation (SD).

averaging 22 nm. In contrast, the GBD system displayed a considerably slower increase (0.06 ± 0.002 Δz-average min$^{-1}$), resulting in an average particle size of only 18 nm.

Compared to previous studies using the covalent SC/ST system (1.53 ± 0.13 Δz-average min$^{-1}$, with a particle size of ≈50 nm)[8] the non-covalent assembly systems, with the exception of the SH3 system, thus showed slower growth rates. These results align to some extent with the lower binding affinity of non-covalent interactions compared to covalent ones. In fact, the reported $K_d$ values of PDZ[18,19] and GBD[20] were 8.0 µM and 1 µM, respectively, while for the SH3 system a $K_d$ value of 100 nM was reported.[14,19] Since these values were determined for different protein species by fluorescence quenching methods, we attempted to measure the binding affinity of the here used enzyme variants by employing isothermal titration calorimetry (ITC). While this did not yield meaningful data for the PDZ and GBD systems despite multiple variations of the analysis protocols (not shown), the ITC investigations of the SH3 system were satisfactory and yielded a $K_d$ value of 24 ± 8 nM (Figure S5, Supporting Information), which was in the same order of magnitude as the literature value.

Unfortunately, no data are currently available on the kinetics and thermodynamics of the assembly of non-covalent protein domains when fused to large enzymes such as those studied here. Consequently, the observed deviations in kinetics and resulting particle sizes, which do not strictly follow the expected affinity-based order (SH3 > GBD > PDZ), together with the discrepancies and challenges in determining the ITC values, suggest that the binding behavior of the three systems is shaped by complex factors introduced by enzyme fusion and the multivalent

interactions inherent to the quaternary structure of the enzymes. In addition, other influences such as steric constraints imposed by the enzyme scaffolds or solvation effects may contribute to these discrepancies. Such effects could alter the accessibility and effective orientation of the binding domains and thereby impact both the rate and stability of assembly in ways that cannot be predicted solely from the affinities of the isolated domains.

### 2.2. Intracellular Production of ncAEH for Biocatalysis Applications

To evaluate the non-covalent interaction systems in biocatalytic flow experiments, we first investigated whether intracellularly produced ncAEH materials could be generated for direct use in biocatalysis. Analogous to previous studies with covalent (SC/ST) AEH,[12] polycistronic plasmids were constructed for the combined expression of the LbADH and BsGDH fusion proteins described above. The co-expression of these binding partners was expected to facilitate their intracellular assembly, leading to the formation of corresponding particles, referred to as inCell-ncAEH. Simultaneously, appropriate negative controls (referred to as "free enzymes") were designed, in which the ligands fused to BsGDH were absent (**Figure 3A**). To determine if cells capable of producing inCell-ncAEH encounter growth challenges following L-arabinose induction, $OD_{600}$ growth curves were initially measured (Figure 3B; Figure S6, Supporting Information). As indicated in Figure 3B, no growth differences were noted prior to induction. However, post-induction, cells expressing inCell-ncAEH entered the stationary phase more rapidly than the control cells expressing only unassembled free enzymes. A similar behaviour was previously observed for the covalent inCell-AEH system.[12] The intracellular production of the respective fusion proteins was confirmed by gel electrophoretic analysis of cell lysates (Figure 3C; Figure S6, Supporting Information). The broad band observed indicated only that the fusion enzymes were successfully expressed inside the cells. Evidence for the actual formation of intracellular ncAEH particles was obtained from the detailed analysis of biocatalytic product formation, as described below.

With the successful expression of enzyme variants, the inCell-ncAEH materials should next be utilized in biocatalytic flow experiments in two distinct formats (Figure 3A). In one approach, the inCell-ncAEH particles were directly immobilized from the cell lysate onto epoxy microparticles that had been functionalized with the complementary binding partner (@beads, Figure 3A). Details on the preparation of the ncAEH@beads are given in Methods Section. In the second approach, whole cells were entrapped within the fluidic reactor after being permeabilized with toluene (@cells, Figure 3A). In both cases, the corresponding beads or cells were loaded in a PTFE reactor (Figure S7, Supporting Information) and subsequently used in a continuous flow setup for the biocatalytic conversion of NDK **1**. The results obtained for the SH3 system are shown in Figure 3D,E. For the inCell-ncAEH@beads materials, only a slight improvement in long-term biocatalytic performance was observed compared to the control samples, which were designed to be unable to form intracellular particles (blue vs gray curve in Figure 3D). The initial conversion of ≈30%, as well as the long-term stability, was significantly lower than the values previously obtained with the corresponding covalent SC/ST materials (> 95% for up to five days).[12] Since the PDZ and GBD systems also did not yield better results (Figure S8, Supporting Information), it was concluded that, despite successful overexpression of inCell-ncAEH proteins, the isolation of intracellularly formed particles by bead extraction is not a viable approach for producing efficient reactor materials.

In the second approach, protein-expressing cells were directly encapsulated in the PTFE reactor as catalytically active material and permeabilized with toluene (for experimental details, see the Methods section). As expected, the results obtained for the SH3 system showed the same initial activity for reactors loaded with inCell-ncAEH@cells as for the control reactors, which were unable to form intracellular ncAEH particles (blue vs gray curve in Figure 3E). However, over the course of the reaction, the performance of the control reactor declined significantly more steeply than that of the inCell-ncAEH@cells reactor (50% vs 10%, respectively). This can be attributed to the gradual washout of enzymes, which occurs significantly more slowly in the presence of assembled particles compared to free enzymes. Indeed, the SH3 system examined here demonstrated excellent performance, maintaining ≈60% NDK conversion even after five days of continuous reaction. This performance was only slightly lower in terms of long-term stability compared to the covalent SC/ST system (≈70% conversion over five days).[12] In contrast, the PDZ and GBD systems exhibited lower initial conversion rates (≈35%) and showed only minor differences compared to the non-assembling controls (Figure S8, Supporting Information).

As an additional indicator for the formation of intracellular ncAEH particles, we conducted a more detailed analysis of product distribution, specifically the ratio of hydroxyketones to diol formation (see Figure 1A). Previous studies had shown that AEH materials produce significantly higher amounts of diol compared to hydroxyketones than free enzymes, as the tight spatial packing of enzymes promotes the two-step reduction of NDK **1**.[8,12] Indeed, a comparison within the SH3 system confirmed this effect: the inCell-ncAEH@cells materials generated nearly twice as much diol as the free enzymes, which was not observed for the PDZ and GBD systems (Figure S9, Supporting Information). These results indicate that the two interacting enzymes are not only closely confined within the hydrogel material, but also that the strength of their non-covalent binding plays a significant role in the formation of ncAEH materials in this format.

Altogether, the studies confirmed that ncAEH materials can be formed intracellularly but also raised doubts about the suitability of such inCell approaches for practical applications. It should be noted that materials formation and catalytic activity may be hindered by interactions with intrinsic *E. coli* proteins. For instance, the SH3 system binds proline-rich motifs, which are present in one-third of *E. coli* proteins, including intrinsically disordered proteins involved in signaling.[23] The PDZ system targets C-terminal sequences in proteins linked to signaling and cytoskeletal anchoring,[24] while GBD plays a crucial role in actin polymerization in *E. coli*.[25] These considerations suggested that the inCell format is not ideal for ncAEH material applications and highlighted the need to explore alternative formulation strategies where optimized enzyme assembly could enhance catalytic activity and stability.

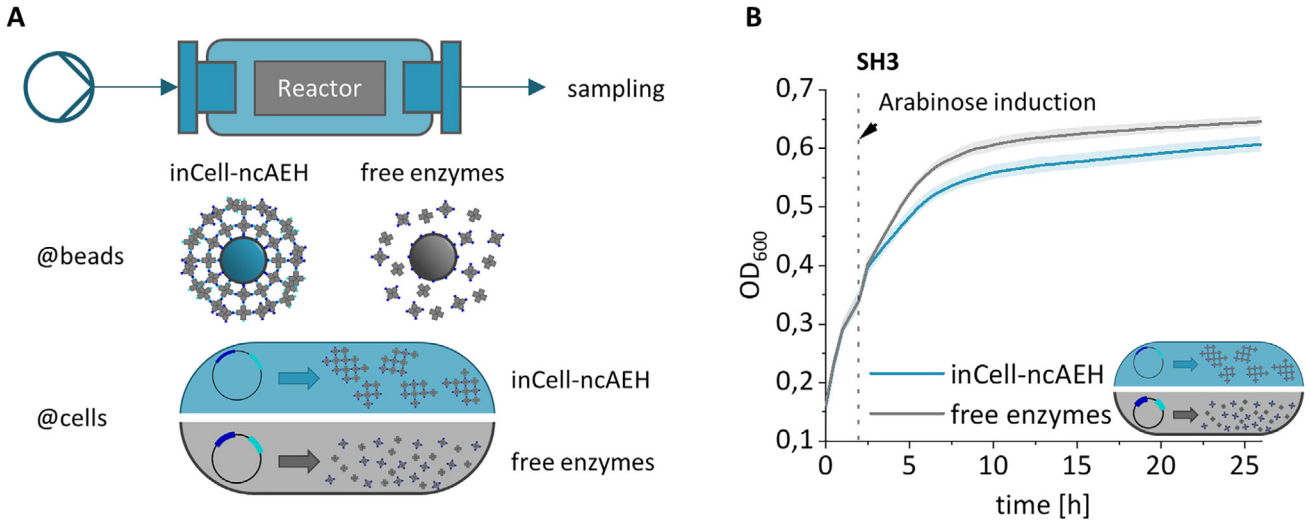


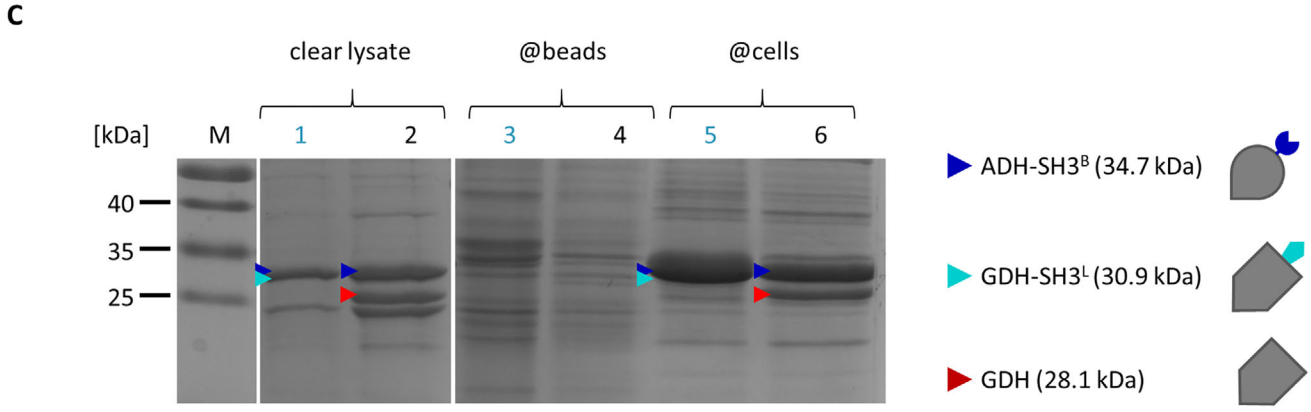


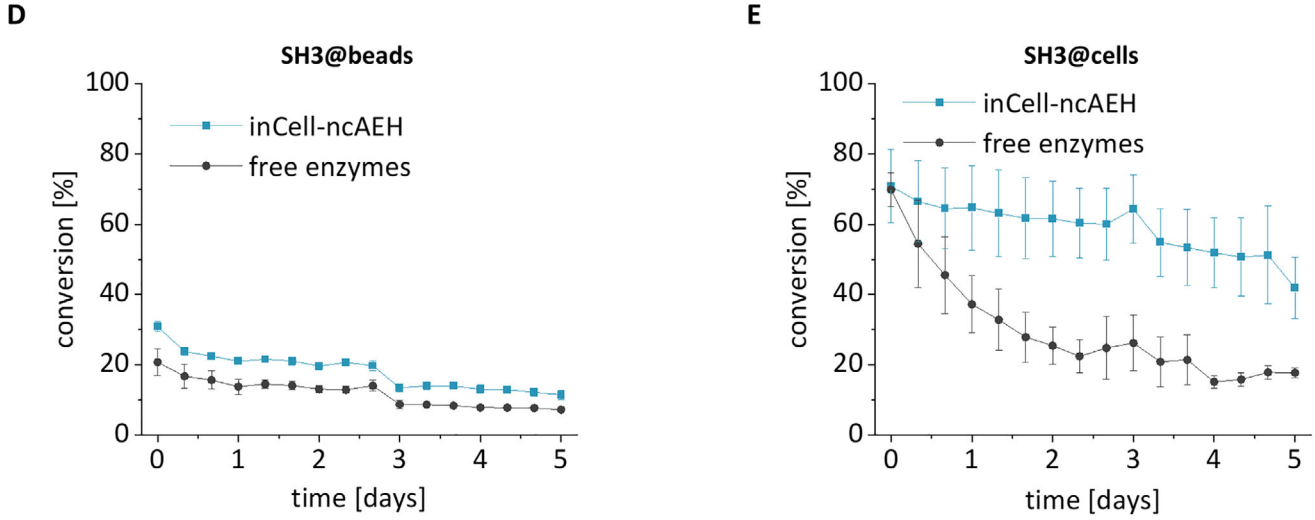

### 2.3. Formulation of ncAEH Materials as Biocatalytic Foams

Next, we investigated whether non-covalent interaction systems could also be used to generate monodisperse, biocatalytically active foams. Unlike the inCell-ncAEH immobilized on beads, this approach would enable carrier-free immobilization, allowing for a higher enzyme loading within the reactor space. To achieve this, the purified protein fusions from Section 2.1 were used to generate monodisperse micro bubbles via a flow-focusing junction, which were then dried into a foam-like material (**Figure 4**).[13] The resulting ncAEH enzyme foams were doped with 100 µM fluorescein isothiocyanate (FITC) before foaming to facilitate characterization via fluorescence microscopy, ensuring homogeneity in shape and pore size.

Freshly prepared ADH-SH3$^{B}$/GDH-SH3$^{L}$ foams exhibited monodisperse, densely packed spherical bubbles (Figure 4Bi), which coagulated into a hexagonal honeycomb network after just 30 min of drying at 30 °C (Figure 4Bii) and remained stable for up to 28 days of extended drying (Figure 4Bv). Analysis using a Python-based script determined an average pore diameter of ≈200 µm throughout the drying process (Figure 4C), while the lamella thickness decreased from ≈12 to 10 µm, leading to material densification (Figure 4D). Similar experiments were conducted with the other non-covalent interaction systems, and both the PDZ and GBD foams exhibited similar behavior during foaming and drying, forming monodisperse spherical bubbles that transitioned into a hexagonal network (Figure S10, Supporting Information). The average pore diameters were 180 µm (PDZ) and 160 µm (GBD), with a consistent lamella thickness of ≈10 µm across all systems. These results correlated well with the previously studied covalent SC/ST-AEH materials,[13] demonstrating that the foaming process can be seamlessly adapted to non-covalent interaction systems. Notably, wild-type enzymes without complementary interaction domains failed to form regular networks upon drying (Figure S10, Supporting Information) and were thus excluded from further analysis.

Direct microscopic validation of the predicted ultrastructure with alternating enzyme building blocks spaced at less than 10 nm is beyond the reach of currently available methods, even with advanced super-resolution techniques. Consequently, we explored indirect approaches to assess enzyme co-localization within the foam matrix. To this end, fluorescence-based co-localization studies were tested using Cy3-labeled ADH-SH3 and Cy5-labeled GDH-SH3, which were incorporated into protein foams via microfluidic foaming and imaged before and after drying (Figure S11, Supporting Information). Fresh foams showed clear enzyme co-localization, whereas drying eliminated the typical honeycomb structure observed for unlabeled proteins (Figure 4B) and caused partial segregation. The absence of a homogeneous superstructure suggests that protein hydrophilicity is a critical factor for foam stability, as the lipophilic dyes may interfere with the SH3-based electrostatic and hydrophobic interactions. While this effect could potentially be mitigated by optimizing foaming and drying conditions, we instead assessed co-localization using a densitometric SDS-PAGE method. Foams of each non-covalent system were prepared and subsequently dissolved in SDS loading buffer (Figures S12–S14, Supporting Information). Quantitative band analysis revealed that both enzymes were present in stoichiometric amounts within the foam matrix, thereby indirectly confirming their co-localization.

### 2.4. Biocatalytic Performance of ncAEH Foams

After confirming that non-covalent binding systems allow the formation of monodisperse foams with a material morphology comparable to those produced via covalent SC/ST interactions, we next aimed to evaluate their catalytic activity and mechanical stability under flow conditions. A key focus was whether ncAEH foams exhibit the enhanced mechanical resilience and prolonged activity observed in covalent AEH foams following the drying process.[13] To experimentally address these questions, four reactors were filled with foams from each non-covalent system (PDZ, GBD and SH3) and dried at 30 °C for different durations (30 min, 2 days, 7 days or 28 days) (**Figure 5**A). The reactors were then integrated into a flow setup (Figure S15, Supporting Information). To evaluate the impact of drying on both mechanical stability and enzymatic activity, four reactors, each subjected to a specific drying duration, were used for the biocatalytic conversion of NDK **1**. The reaction was conducted over 30 h using four different flow rates (1, 2, 5, and 10 µL min$^{-1}$, Figure 5B). Since higher flow rates impose greater shear stress and mechanical load on the ncAEH foams, this experiment enabled a direct evaluation of both their material stability and catalytic performance.

As shown in Figure 5B, NDK conversion remained nearly quantitative at the low flow rate of 1 µL min$^{-1}$ throughout the entire observation period. However, increasing the flow rate caused a rapid decline in conversion efficiency, with the extent of the drop depending on the applied flow rate. Higher flow rates led to faster declines and lower final conversions, consistent with loss of ncAEH material due to hydrostatic pressure flushing it out of

**Figure 3.** Characterization of inCell-ncAEH as biocatalytic reactor materials exemplarily shown for the SH3 system. The corresponding data for the PDZ and GBD systems are shown in Figures S6 and S8 (Supporting Information). A) Schematic illustration of the two approaches used to test inCell-ncAEH in continuous flow biocatalysis. Intracellularly produced inCell-ncAEH particles were extracted from crude cell lysates on pre-functionalized microparticles (@beads) or used as whole E. coli cells, permeabilized with 5% toluene (@cells). Note that controls were used in both formats in which the ligands fused to BsGDH were absent. B) $OD_{600}$ growth curves of E. coli cells expressing the inCell-ncAEH and free enzymes. C) 16% coomassie stained SDS-PAGE analysis of clear lysates of cells expressing the inCell-ncAEH (lane 1) and free enzymes (lane 2) to be used for the immobilization on microparticles. Analysis of the beads loaded with inCell-ncAEH (lane 3) and free enzymes (lane 4) did not indicate successful loading of substantial amounts of enzymes, although intracellular overexpression clearly occurred (lanes 1 and 2). In case of lysed inCell-ncAEH cells (lane 5) overexpression of ADH-SH3$^{B}$ (34.7 kDa, blue arrow) and GDH-SH3$^{L}$ (30.9 kDa, turquois arrow) resulted in one broad band, suggesting a similar electrophoretic mobility of the two proteins. The control with free enzymes (lane 6) shows the expected overexpression of ADH-SH3$^{B}$ (34.7 kDa, blue arrow) as well as of GDH (28.1 kDa, red arrow) lacking the SH3$^{L}$. D) Biocatalytic conversion of NDK 1 to the corresponding products using bioreactors containing either inCell-ncAEH@beads (blue) or free enzymes@beads (grey). E) Conversion of NDK 1 using bioreactors loaded with inCell-ncAEH@cells (blue) or free enzymes@cells (grey). Biocatalysis reactions were carried out at a flow rate of 5 µL min$^{-1}$ for 5 days. Sample size (n): C), D) n≥2. All error bars represent the standard deviation (SD).

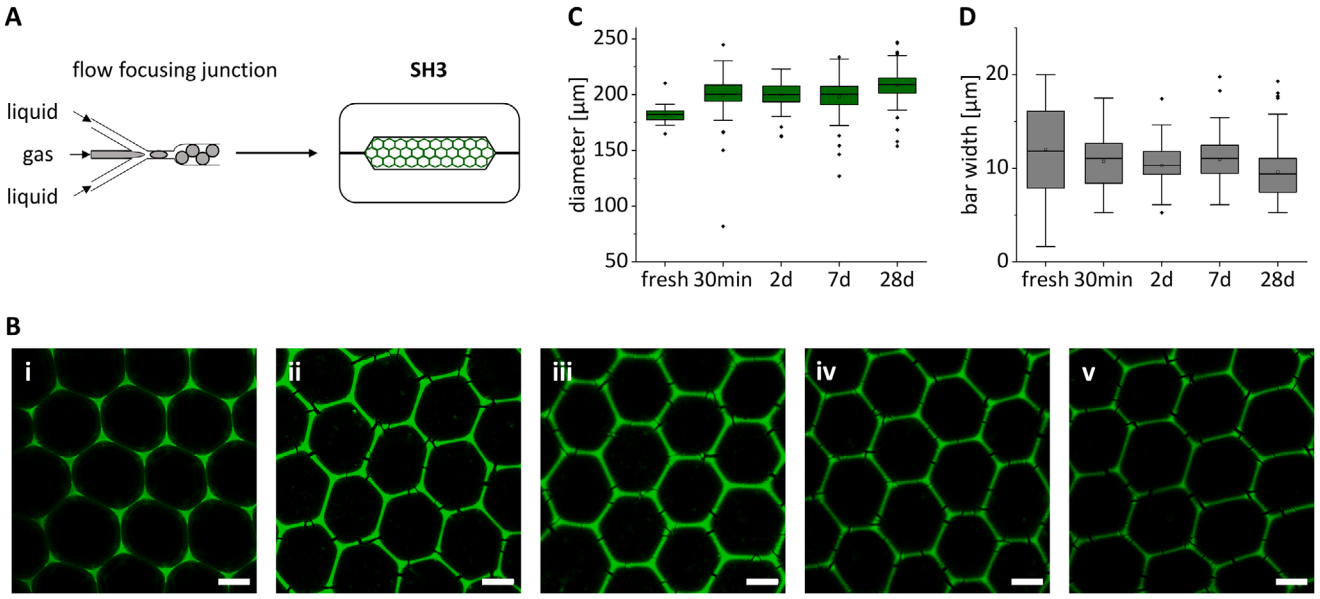


**Figure 4.** Structural characterization of enzyme foams consisting of ncAEH materials based on the SH3 system. A) Schematic illustration of micro bubble production with a flow focusing junction, which allows the monodisperse foam to be filled directly into microfluidic reactors and dried therein before usage in biocatalytic experiments. Two streams of an aqueous solution containing equimolar concentrations of the complementary ADH$^{B}$ and GDH$^{L}$ proteins (1 mM) intersect with an $N_2$ gas stream at defined pressure rates of 450 mbar (liquid) to 400 mbar (gas). B) Fluorescence microscopy images of FITC labeled enzyme foams subjected to variable times of drying (i = fresh, ii = 30 min, iii = 2 d, iv = 7 d, v = 28 d) at 30 °C. Scale bars: 100 µm. Boxplot diagram of pore diameter distribution C) and average web widths in the lamellae D) for the corresponding drying times. Sample size (n): C) n≥20, D) n>70.

the reactor. The comparison of endpoint conversions after 30 h of continuous catalysis for different drying times and flow rates (Figure 5C) clearly showed that extended drying durations enhanced the biocatalytic stability of the material. These findings align with our conclusion that the mechanical stability of the protein foams increases during drying and is directly linked to the affinity of the non-covalent interaction domains. Stability can be maximized when this affinity approaches covalent strength, which in turn enables higher productivity at elevated flow rates in continuous processes.

Similar trends were observed for the other non-covalent interaction systems. While GBD-based ncAEH foams demonstrated significantly lower overall performance, a subtle drying effect was still noticeable (Figure 5D). The generally low coupled activity of the GBD-based ncAEH material (Figure 2B) likely stems from the minimal activity of the ADH-GBD$^{B}$ component (Figure 2A). Interestingly, PDZ-based ncAEH foams showed a strong drying effect, markedly enhancing both stability and productivity (Figure 5E), nearly matching the SH3 system (Figure 5C). While the superior stability of the SH3 material was anticipated due to the high-affinity interaction, this advantage appears to be offset by the lower activity of the SH3 enzyme variants (Figure 2B). Hence, these results demonstrate that maximizing foam stability through extended drying and the use of high-affinity interaction domains is key to sustaining high catalytic performance in continuous-flow operation, even at elevated flow rates.

To further evaluate the mechanical stability of the different ncAEH foams, independent of their catalytic activity, fluorescence microscopy analysis was performed after 30 h of continuous operation in the reactor (Figure 5F–H). Both SH3- and PDZ-based foams retained intact hexagonal structural regions, whereas GBD foams were almost entirely washed out. A direct comparison between SH3 and PDZ foams revealed that SH3 foams retained their characteristic thin struts between pores, while PDZ foams appeared significantly more swollen, likely due to their weaker interaction strength. These findings highlight the crucial role of interaction strength in maintaining the structural integrity of ncAEH foams under continuous flow conditions. While SH3-based foams demonstrated superior mechanical stability, the pronounced swelling of PDZ foams suggests that optimizing interaction properties could further enhance material robustness and performance.

In summary, the three investigated non-covalent binding systems demonstrated their ability to efficiently form monodisperse enzyme foams, all of which exhibited the drying-induced aging effect previously observed in covalently crosslinked AEH foams via SC/ST interactions. Although the GBD system was unsuitable for the enzymes tested, both the weak-binding PDZ and the much stronger SH3 systems yielded stable ncAEH foams that operated at a practical flow rate of 10 µL min$^{-1}$, achieving conversion rates comparable to covalently crosslinked AEH foams.

To place these results in the context of benchmarking and potential optimization, we conducted preliminary experiments varying the relative amounts of ADH-SH3$^{B}$ and GDH-SH3$^{L}$ in batch solution (Figure S20, Supporting Information). The results showed that i) foams had lower activity than free enzymes, ii) adjusting enzyme ratios could improve catalytic performance by about twofold, and iii) this effect was independent of whether

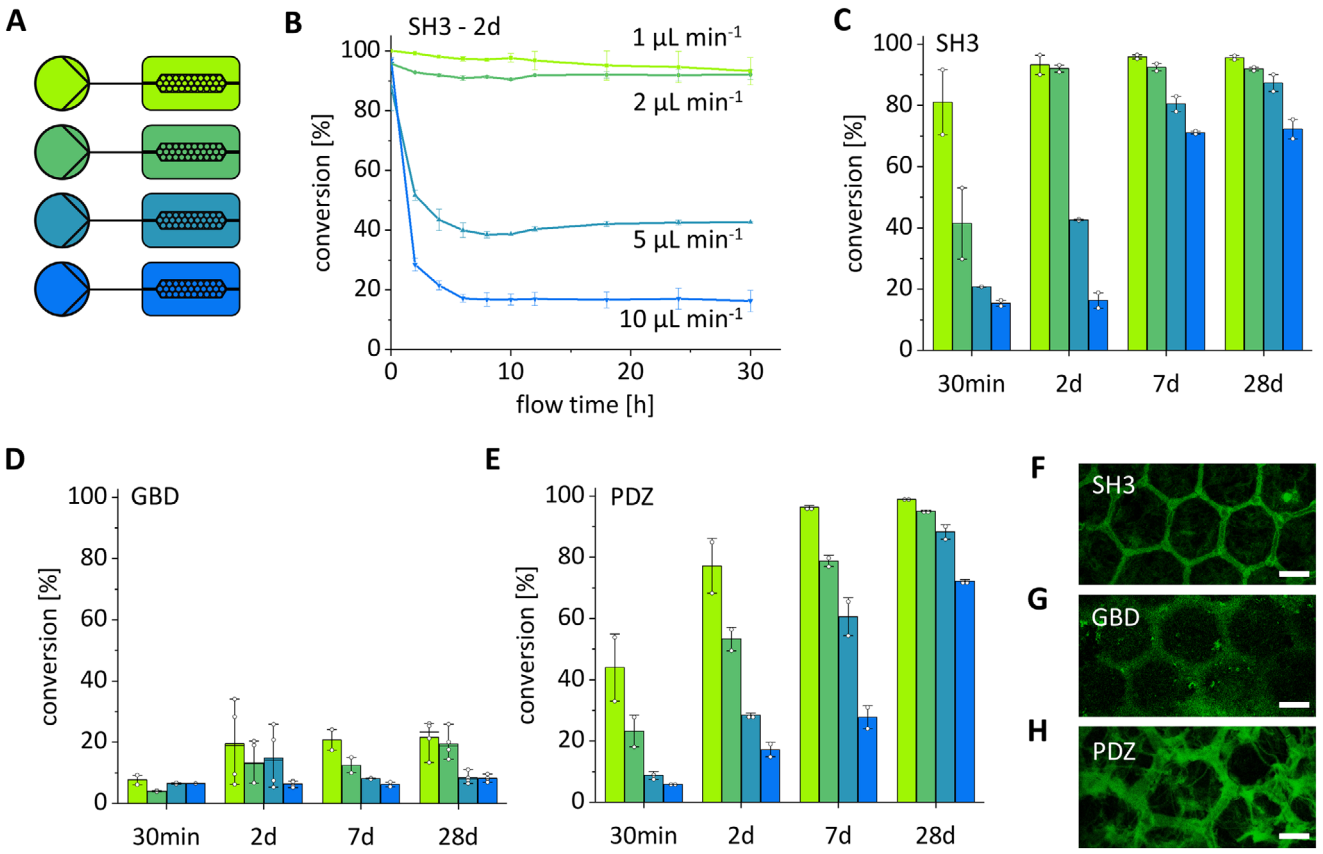


**Figure 5.** Catalytic performance and durability of SH3-based ncAEH foams in continuous flow biocatalysis. A) Schematic drawing of experimental setup. PDMS microreactors loaded with enzyme foams were subjected to drying for variable time periods (30 min, 2 days, 7 days or 28 days). To assess the impact of drying on both the enzymatic activity and mechanical stability, the reactors were then used to conduct the NDK model reaction at variable flow rates. B) Flow rate-dependent NDK conversion observed in SH3 ncAEH foam reactors that were dried for 2 days. Note that the curves represent substrate turnover, determined via product formation (see also Figure S16, Supporting Information). The observed decrease in turnover over time reflects the gradual decline in catalytic productivity. C) Endpoint values of biocatalytic conversion observed after 30 h of continuous catalysis for the variable drying times and flow rates applied. D,E) Endpoint conversion data, similar to that in C), observed for reactors containing GBD- and PDZ-based ncAEH foams. Note that the bars indicate product formation, with the corresponding profiles for hydroxyketone and diol shown in Figure S16 (Supporting Information). F-H) Representative fluorescence microscopy images of ncAEH foams dried for 28 days, following 30 h of perfusion under continuous flow conditions, for SH3- (F), GBD- (G), and PDZ- (H)-based materials. Scale bars: 100 µm. Sample size (n): C – E) n≥2. All error bars represent the standard deviation (SD). For the detailed data on drying time- and flow rate-dependent NDK conversion, see Figures S17–S19 (Supporting Information).

the enzymes were free or immobilized as hydrogel foams. We also compared specific activities for all coupling systems at a 1:1 ADH:GDH ratio in free and foam formats. The GBD system showed almost no activity in either format, while SH3 and PDZ systems retained 40–60% of free-enzyme activity after foam formulation (Figure S21A, Supporting Information). Importantly, whereas foams maintained their activity, free enzymes exhibited complete loss of activity within 2 days (Figure S21B, Supporting Information). While these experiments were performed with enzyme materials in the batch format, the true advantage of the foam materials lies in their ability to be dried and subsequently used in continuous-flow operation, where their stability and tunability can be fully exploited. Taken together, these results highlight the potential of foam-based immobilization not only to maintain activity over time but also to be tailored for improved performance, with optimized formulations offering the prospect of combining long-term stability with high catalytic efficiency in continuous processes.

For benchmarking the non-covalent biocatalytic foam materials developed in this study, we took advantage of the NDK conversion model system, which we had previously used for quantitative comparisons of various heterogeneous continuous-flow biocatalysis formats.[11] In earlier work, we compared the volumetric performance, expressed as space–time yields (STYs), of self-assembled monolithic ADH–GDH hydrogel materials assembled via covalent SC/ST interactions[8] with several conventional immobilization strategies. These included physisorption or chemical crosslinking to polystyrene surfaces, a packed-bed reactor with enzymes immobilized on magnetic particles, and a living *E. coli* biofilm catalyst expressing ADH and GDH.[11] Among these, the monolithic ADH–GDH hydrogels achieved by far the highest STY, outperforming the next-best approach, enzyme immobilization on beads, by approximately fivefold.[11] To place the non-covalent foam-based systems assembled with either SH3 or PDZ interaction modules into this context, they were benchmarked against analogous foam materials

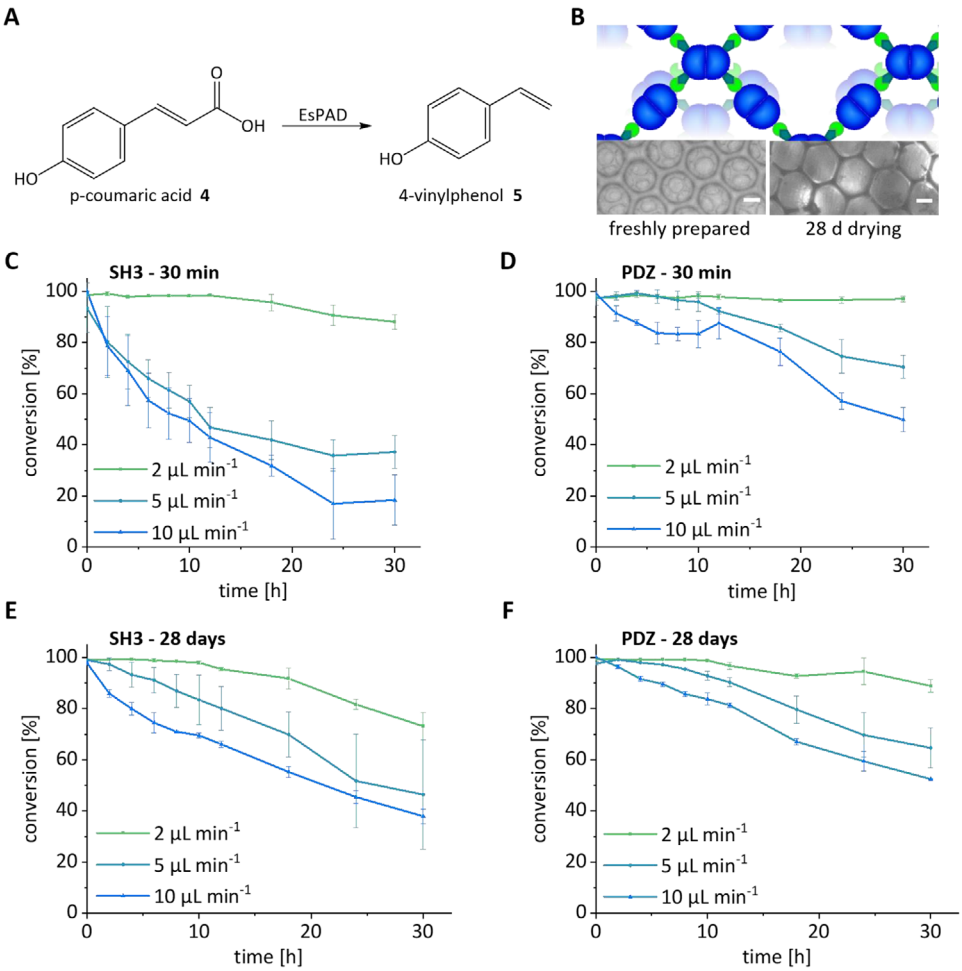


**Figure 6.** Characterization of ncAEH materials made of the homodimeric EsPAD enzyme. A) Reaction scheme of the EsPAD catalyzed conversion of p-coumaric acid 4 to 4-vinylphenol 5. B) Schematic illustration of ncAEH structure of the enzyme crosslinking (top) and transmitted light microscopy images (bottom) of a freshly prepared (left) and 28 days dried (right) foam based on the SH3 interaction system. Note that the cartoon shows a simplified, idealized structure. C-F) Biocatalytic conversion of 4 in time-course experiments over 30 h of continuous flow catalysis at variable flow rates using reactors with SH3- (C, E) or PDZ- (D, F)-based ncAEH foams, dried for either 30 min (C, D) or 28 days (E, F). Scale bars: 100 µm. Sample size (n): C – F) n≥2. All error bars represent the standard deviation (SD).

assembled via covalent SC/ST interactions[13] and against the aforementioned monolithic AEH materials assembled via covalent SC/ST interactions.[8] The results show that the foam systems consistently outperformed monolithic AEH materials by about twofold, with covalently and non-covalently linked foams displaying comparable STYs. Both foam formats achieved STY values of ≈180 g $d^{-1}$ $L^{-1}$ at a flow rate of 10 µL $min^{-1}$ (Figure S22, Supporting Information).

Building on this internal benchmarking, we also compared the ncAEH foams to performance values typically cited for economically viable biocatalytic processes. In industrial applications, operational stability is often defined by a minimum runtime of 5–10 h.[26] With a catalytic runtime of 30 h, our system clearly surpasses this criterion. Reported STYs for high-performing ketoreductases in the synthesis of the chiral alcohol moiety of atorvastatin can reach up to 1000 g $d^{-1}$ $L^{-1}$,[2] whereas the minimum industrial requirement is >16 g $d^{-1}$ $L^{-1}$.[2] The ncAEH foams presented here achieve STYs approaching 200 g $d^{-1}$ $L^{-1}$, well above this threshold. Given that enzymes used in industrial processes are frequently optimized through protein engineering, we are confident that the performance of the protein foams could be further enhanced using similar strategies.

### 2.5. Exploring Enzyme-Based Material Connectivity – The Case of Phenolic Acid Decarboxylase

Finally, we aimed to evaluate the transferability of the described concept to other enzymes lacking a tetrameric tertiary structure. For this purpose, we selected the phenolic acid decarboxylase from *Enterobacter sp.* (EsPAD), which catalyzes the enzymatic conversion of p-coumaric acid **4** to 4-vinylphenol **5** (**Figure 6A**). Unlike the previously tested ADH and GDH enzymes, EsPAD forms a homodimer instead of a homotetramer. Hence, to compensate for the absence of a tetravalent enzyme scaffold while ensuring the formation of a highly crosslinked

ncAEH material, a modified EsPAD variant with two binding sites per monomer was required. Based on previous studies on covalent AEH materials,[10] plasmids were designed for the expression of EsPAD variants. In the SH3 system, a bivalent monomer was constructed, featuring two binding domains at the N- and C-terminus ($SH3^B$-EsPAD-$SH3^B$), while a monovalent variant was created with the SH3 ligand fused only to the C-terminus (EsPAD-$SH3^L$). Similarly, for the PDZ system, a bivalent monomer was designed with two PDZ ligands at the N- and C-terminus ($PDZ^L$-EsPAD-$PDZ^L$), whereas the PDZ binding domain was fused only to the C-terminus in the monovalent variant (EsPAD-$PDZ^B$). Given the low performance of the GBD interaction system in the previous ADH/GDH studies, it was not included in this investigation.

All variants were recombinantly expressed in E. coli and purified to homogeneity via chromatography (Figure S23A, Supporting Information). Enzymatic activity analysis revealed no significant differences among the four new EsPAD variants compared to the wild-type EsPAD (Figure S23B,C, Supporting Information). To assess their suitability as enzyme building blocks for ncAEH foam production, equimolar solutions in respect to the ligand and ligand-binding domains of the four variants were mixed and microfluidically foamed under the same conditions as the LbADH/BsGDH system. Microscopic examination of both freshly foamed suspensions and foams dried for 28 days showed no notable differences from LbADH/BsGDH foams, despite variations in enzyme-based linkage geometry and material connectivity (Figure 6B).

After successfully formulating ncAEH EsPAD foams, the dried materials (aged for 30 min or 28 days) were tested in flow reactors at variable flow rates of 2, 5, and 10 µL $min^{-1}$ for the conversion of p-coumaric acid. Chromatographic analysis of conversion rates for the SH3- and PDZ-based foams dried for 30 min is shown in Figure 6C,D, respectively. At a low flow rate of 2 µL $min^{-1}$, both systems achieved nearly quantitative conversion with comparable efficiency. However, as the flow rate increased to 10 µL $min^{-1}$, the PDZ system demonstrated greater robustness despite its interaction affinity being over 100 times weaker than that of the SH3 system. The impact of prolonged drying (28 days) on conversion rates, illustrated in Figure 6E (SH3) and 6F (PDZ), clearly highlights the stabilization of the foam network against mechanical stress. Under continuous perfusion for 30 h at the practically relevant velocity of 10 µL $min^{-1}$, both systems exhibited intermediate conversion rates of ≈50%. Compared to previously studied covalently crosslinked monolithic AEHs,[10] the non-covalent EsPAD foams showed equivalent catalytic activity, reaching a STY of ≈60 g $d^{-1}$ $L^{-1}$ (PDZ), highlighting the efficiency and potential of biocatalytic foams. In addition, batch experiments comparing the specific activities of free enzymes and EsPAD foams (Figure S24, Supporting Information) showed an average retained activity of 50%, which is consistent with the values observed for the ADH/GDH system (Figure S21, Supporting Information).

Surprisingly, however, the weaker PDZ system exhibited a lower stabilization effect than the stronger SH3 system (Figure 6C,E vs D, F), suggesting that in this enzyme system, higher binding affinity benefits more from the drying process. This effect was not observed in the ADH/GDH enzyme system, highlighting the crucial role of enzyme properties in determining the structural integrity of the foams. It seems that not only the designed non-covalent interactions but also the intrinsic self-assembly properties of the enzyme building blocks contribute to the overall material stability. The linear decline in catalytic performance observed for EsPAD foams suggests a more gradual structural degradation, whereas the exponential drop in activity for ADH/GDH foams points to a more fragile network, potentially due to weaker or more dynamic multimerization interactions. These differences emphasize that the mechanical resilience of ncAEH materials cannot be solely attributed to their affinity-based interaction domains but must also account for the inherent quaternary structure and stability of the enzymes themselves. Although experimental quantification of these interaction forces within the systems remains out of reach, understanding these effects could enable targeted optimization strategies, such as protein engineering or cross-linking approaches, to enhance material durability and long-term performance in continuous flow applications.

## 3. Conclusion

Our work demonstrates the first successful integration of non-covalent binding systems (SH3, GBD, PDZ) into biocatalytically active all-enzyme hydrogels (AEHs) for flow biocatalysis. The influence of protein fusions on ADH activity highlights the necessity of diverse coupling strategies beyond established covalent SC/ST-based AEHs. Despite affinities varying over two orders of magnitude (SH3 > GBD > PDZ), optimized systems based on SH3 and PDZ enabled stable conversions of >70% over 30 h in continuously perfused reactors. Notably, carrier-free enzyme foams revealed that drying significantly enhanced mechanical stability and enzymatic activity, making these ncAEH foams highly promising for reactor applications. Additionally, non-covalent systems were successfully transferred from the homo-tetrameric ADH/GDH to a homo-dimeric phenolic acid decarboxylase (EsPAD), demonstrating their versatility and adaptability. Given their flexibility, ease of implementation, and stabilization effects, non-covalent binding systems present a powerful approach for developing robust enzyme-based materials, paving the way for sustainable industrial biocatalysis.

## 4. Experimental Section

*Genetic Construction of Plasmids for Protein Expression*: For genetic constructs that required the introduction of large gene segments (>100 bp), the isothermal recombination described by Gibson et al.[27] was used. Short gene inserts or modifications were inserted directly in the vector backbone by using PCR with specifically designed primers. After the Gibson assembly or the polymerase chain reaction (PCR), the reaction mixtures were treated with DpnI to remove any remaining vector template and then transformed into *E. coli DH5α* cells. All plasmids were purified using ZR Plasmid Miniprep–Classic (Zymo Research, Germany) according to the manufacturer's instructions. Correct assembly and sequence of the desired constructs was verified by commercial sequencing (LGC genomics, Germany). The used primers were ordered from Sigma Aldrich and inserts were designed and ordered by the Invitrogen GeneArt Strings DNA Fragments service of ThermoFisher Scientific.

The genetic constructs were designed with the non-covalent binding domains ($PDZ^B$, $GBD^B$ and $SH3^B$) separated from the enzyme gene by a GGGGS linker, while the ligands ($PDZ^L$, $GBD^L$ and $SH3^L$) were separated from the enzyme gene by a longer GGGGSGGGGS linker. The 6xHis-tag

at the C- or N-term was separated from the gene by a G residue. In case of the inCell-ncAEH vectors, the two fusion proteins were separated by a second RBS region as previously reported.[12]

All genetic constructs, used primers and the summarized genetic construction protocol are listed in Tables S1–S4 (Supporting Information).

*Protein Expression and Purification*: Protein production was carried out as previously described.[8,12] In brief, 2.5 L overnight cultures starting from individual *E. coli* BL21 (DE3) colonies carrying the respective plasmids were harvested by centrifugation (10 000 g, 10 min, 4 °C), resuspended in 20 mL $NP_i$-10 buffer (50 mM $NaH_2PO_4$, 500 mM NaCl, 10 mM Imidazole, pH 8.0). The cells were lysed by ultrasonication, the cell debris removed by centrifugation (45 000 g, 1 h, 4 °C) and the supernatant was filtered through a 0.45 µm Durapore PVDF membrane (Steriflip, Millipore) and loaded on a HisTrap FF (5 mL) Ni-NTA column (GE Healthcare, Germany) mounted on an Äkta Pure liquid chromatography system (GE Healthcare, Germany). After washing with 100 mL $NP_i$-10 buffer, the 6xHis-tagged proteins were eluted using a gradient from 100% $NP_i$-10 buffer to 100% $NP_i$-500 buffer (50 mM $NaH_2PO_4$, 500 mM NaCl, 500 mM Imidazole, pH 8.0). Subsequently, the buffer was exchanged to KMB (100 mM $KP_i$ pH 7.5, 1 mM $MgCl_2$) using Vivaspin 10 000 MWCO (GE Healthcare). The purified proteins were analyzed by standard discontinuous SDS-polyacrylamide Laemmli-midi-gels with Coomassie staining and the molecular mass was compared to the Color Prestained Protein ladder, Broad Range (New England Biolabs). The concentrations were determined by UV–vis spectroscopy, using the theoretical molar extinction coefficients at 280 nm, as calculated by the Geneious version 9.1.3 software.[28] Note that all pET-vectors contain an Ampicillin resistance and were induced using 0.1 mM IPTG. The pTF16-plasmids in contrast have a Chloramphenicol resistance and were induced with 5 mM arabinose. Further, for all EsPAD constructs buffer was exchanged to KMB containing 150 mM NaCl.

*Determination of Enzymatic Activity*: The specific activities of LbADH and BsGDH fused enzymes were determined as previously described.[29] In brief, enzyme assays were performed with a reaction mixture containing 5 mM NDK **1**, 100 mM glucose, 1 mM $NADP^+$, in KMB (100 mM potassium phosphate, pH 7.5, 1 mM $MgCl_2$) containing 0.5 µM of the LbADH fused to the corresponding non-covalent binding domain and an excess of 10 µM GDH-His for NADPH-regeneration. The GDH-containing reaction mixture was preincubated for at least 30 min at 30 °C prior to the addition of the ketoreductase. For the determination of the average specific activity, samples for HPLC analysis were taken after 20 min, while for the determination of enzyme kinetics, reactions were carried out for 24 h. Samples were taken manually at various time points and were subsequently analyzed by chiral HPLC. In order to measure the activity of BsGDH-fusion proteins, 0.5 µM of the respective tagged GDH was incubated together with an excess of 10 µM His-LbADH, using the same conditions as described above for the ketoreductase kinetics. To assess the coupled enzymatic activity, ADH and GDH were added in equimolar amounts, each with a final concentration of 0.5 µM. Note, that due to low enzymatic activity of the ADH-$GBD^B$ component a final concentration of 10 µM was used to determine the coupled activity within the GBD-system. For HPLC analysis, 50 µL of the crude reaction mixtures were extracted with 150 µL ethyl acetate, centrifuged for phase separation, and 30 µL of the organic phase were transferred into 96-nunc well plates and evaporated (Concentrator plus, Eppendorf). Chiral HPLC analyzes were carried out as described later. Values for conversion, enantiomeric and diastereomeric excess were calculated based on the peak intensity of HPLC signals of the substrate and products detected at 210 nm, as previously described.[30] The enzymatic activity can also be given in U, which was equal to $\mu mol_{substrate}\ min^{-1}$.

The decarboxylase activity of the EsPAD variants was measured as previously described.[31] with minor modifications. Briefly, 1 mL of 5 mM *p*-coumaric acid dissolved in 100 mM KMB (pH 7.5, 1 mM $MgCl_2$, 150 mM NaCl) was incubated at 30 °C with 500 rpm shaking. The reaction was initiated by addition of 5 µL of enzyme solution prepared in the same buffer, yielding a final enzyme concentration of 0.3 µM. At defined time points, 100 µL of the reaction were sampled and quenched by mixing with 300 µL of a 2:1 (v/v) mixture of acetonitrile and aqueous 0.1% trifluoroacetic acid. The samples were then centrifuged and the supernatant was transferred to HPLC vials for further analysis. Measurements were run on one biological replicate with $n \geq 2$ technical replicates in parallel.

*Dynamic Light Scattering*: For DLS measurements of purified protein samples 100 µL of purified protein solution was transferred into UV-cuvettes. Loaded cuvettes were placed in a Nano-Series ZetaSizer Nano ZSP (Malvern Instruments, UK) equipped with a He–Ne-Laser (633 nm). Before measurements proteins were centrifuged at 25 °C for 5 min at 10000 rpm. The concentration of the supernatant was measured and set to 0.5 mM. Subsequently the average hydrodynamic radius of the protein particles (z-average), calculated from the auto-correlated light intensity data using the ZetaSizer software, was measured over a time course of 3 h with data acquisition every 100 sec. The nanogel formation kinetics ($\Delta$z-average $min^{-1}$) were calculated based on the linear increase of the z-average for each system respectively.

*Isothermal Titration Calorimetry*: ITC measurements of purified proteins were carried out as described before.[32] In brief, the cell was loaded with $SH3^B$ at a concentration of 20 µM and the syringe with the $SH3^L$ at 200 µM, respectively. For the required control experiments either the cell, the syringe or both were loaded with KMB (100 mM potassium phosphate, pH 7.5, 1 mM $MgCl_2$). Afterwards standard ITC-BIND experiments were performed.

*Growth Curves*: To obtain high-resolution growth curves, inoculation cultures were cultivated overnight in TB medium containing 25 µg $mL^{-1}$ chloramphenicol as a selection marker ($TB_{Cm}$) at 37 °C with shaking at 180 rpm. These overnight cultures were then used to inoculate 5 mL of fresh $TB_{Cm}$ and grown until they reached an $OD_{600}$ of 0.6 – 0.8. The cultures were subsequently diluted to an $OD_{600}$ of 0.1 and transferred to a 96-well plate. Measurements were taken every hour using a Synergy H1 reader (BioTek Instruments, Germany), and after 2 h, the cultures were induced with 5 mM arabinose.

*Immobilization on Epoxide Microparticles and Application for Flow Biocatalysis*: For immobilization of the inCell-ncAEH out of crude extracts, 15 mg of commercially available epoxide activated microparticles (Profinity Beads, Bio-Rad) were functionalized with the corresponding non-covalent binding domain as previously reported.[29] In brief, 100 µL of a 1 mM solution of the non-covalent binding domain was added to the beads and incubated at RT for 2 h and continuous rotation. Afterwards the beads were washed three times with 1 mL KMB, then transferred into the clear lysate and incubated for 1 h at 4 °C and rotation. Subsequently the microparticles were washed three times with 5 mL KMB (100 mM potassium phosphate, pH 7.5, 1 mM $MgCl_2$) each. Finally, the microparticles were resuspended in 100 µL KMB and loaded into the PTFE-based reaction chamber.

*Toluene Permeabilization of E. coli Cells and Application for Flow Biocatalysis*: The permeabilization and application for flowbiocatalysis was done as previously described.[12] In brief, *E. coli* BL21 (DE3) cells harboring the control or inCell-ncAEH vectors were inoculated into 30 mL $TB_{Cm}$ and cultivated overnight at 37 °C and 180 rpm. The next day, 2 mL of these cultures were used to inoculate 100 mL $TB_{Cm}$ at 37 °C and 180 rpm until an optical density of 0.6–0.8 was reached. Subsequently the cells were induced with arabinose to a final concentration of 5 mM and incubated overnight at 25 °C and 180 rpm for protein expression and inCell-ncAEH formation. The induced cells were centrifuged and resuspended in KMB (100 mM potassium phosphate, pH 7.5, 1 mM $MgCl_2$) to a final cell density $OD_{600}$ of 10. To permeate the cells, 25 µL of toluene was added to 475 µL of cell suspension and incubated at 4 °C for 30 min. After treatment the cells were washed 3 times with 1 mL KMB. Finally, the permeabilized cells were resuspended in 500 µL KMB and 100 µL of this suspension were loaded into the PTFE-based reaction chamber.

*Microreactor Preparation*: The microfluidic reactor was prepared as previously described.[8] In brief, the upper part containing the reaction channel was manufactured by replica casting of polydimethylsiloxane (PDMS) (Sylgard 184, Dow Corning, USA) in brass replication molds. The straight channel was 3 mm wide, 1 mm high and 27 mm long with a total volume of 75 µL. Cannulas (Sterican, B. Braun Melsungen AG, Germany) were inserted through horizontal holes in the molds before pouring the PDMS prepolymer to serve as placeholders for the cannulas. The PDMS was cured at 60 °C for at least 3 h.

*Production of Enzyme Foams and Application for Flow Biocatalysis*: The flow focusing junction was produced by a milling machine (Mini Mill GX, Minitech Machinery, USA) from cut sheets of polymethyl methacrylate (PMMA). The junction design was created using a CAD (computer-aided design, Inventor Professional 2018, Autodesk). The channel dimensions were already described in other studies.[33] and were adopted for our purposes. By introducing nitrogen into the two reservoirs, a pressure was generated which, in the case of the liquid phase reservoir, forces the enzyme solution present into the flow-focusing junction with a definable flowrate. "EZ flow" microfluidic pressure control systems (Fluigent GMBH, Jena, Germany) were used to regulate the pressure. These were connected by means of a socket and the appropriate connections (diameter 0.5 mm, Bohlender GMBH, Grünsfeld, Germany) in which the flow focusing junction was clamped. This setup was placed on an Olympus CKX41 microscope (Olympus Europa SE & Co. KG, Hamburg, Germany). Through its objective, the flow focusing junction could be observed and digitally recorded in real time by a screw-mounted Ximea MQ003MG-CM high-speed camera (Ximea GmbH, Münster, Germany).

The catalytically active protein foam was prepared as already described.[13] In brief, an aqueous solution containing equimolar amounts of the two enzymes (500 µM each in KMB) was incubated on ice for 5 min. Subsequently, the protein solution was connected to the flow focusing junction as described above and foamed with constant pressures of 450 mbar for the liquid phase and 400 mbar for the gas phase. The outflowing monodisperse microbubbles were directly collected in PDMS microreactors and dried at 30 °C until further use.

The microfluidic setup was used as described in previous works.[13] The PDMS reactor chips were sealed with a polyolefin foil (HJ-BIOANALYTIK GmbH, Germany). Up to eight low pressure pumping units (CETONI, Germany) equipped with 30 mL Omnifix syringes (B. Braun Melsungen AG, Germany) were connected to the chip for perfusion of reaction media at a respective flowrate of 1, 2, 5 or 10 µL $min^{-1}$. The syringes were filled with 5–25 mL substrate solution containing 5 mM of substrate (NDK 1) and 100 mM glucose in KMB, supplemented with 0.01% (v/v) sodium azid to avoid fouling and 1 mM $NADP^+$. The chip outflow was connected to the rotAXYS360 system (CETONI, Germany) to allow for automatic fractioning into 96-well plates, already loaded with 50 µL 7 M $CH_5N_3$-HCl to stop all enzymatic reactions. The pumps and the positioning system were connected to a CETONI neMESYS Base module, which was controlled by the QmixElements-Software. The chip was connected to syringes and the fraction collector by tubings (Inlets: silicone Tygon tubing R3603, ID = 1.6 mm, Saint-Gobain, France; outlets: conventional PTFE tubing, ID = 0.5 mm) using standard cannulas and luer lock fittings. Please note that, in terms of using EsPAD-based foams the substrate mixture contained 5 mM *p*-coumaric acid **4** in KMB supplemented with 0.01% (v/v) sodium azid to avoid fouling. 100 µL chip outflow was quenched with 300 µL stop solution (2:1 (m/v) mixture of pronaediol and 0.1% TFA in $H_2O$) preloaded into 96-well plates. For sample preparation for HPLC analysis 150 µL from each well was mixed in an Eppendorf tube with equal volume of acetonitrile. Afterwards this mixture was centrifuged for 5 min at 16000 g and 250 µL were transferred to HPLC vials.

*Fluorescence Labelling of ADH and GDH*: The enzymes were labeled by adding an eightfold molar excess of fluorescent dye. Specifically, ADH-$SH3^B$ was incubated with an NHS-activated Cy3 and GDH-$SH3^L$ with an NHS-activated Cy5. The labeling reaction was carried out overnight at 4 °C under continuous mixing to ensure efficient conjugation. On the following day, unbound fluorescent dyes were removed using VivaSpin centrifugal filters, resulting in the isolation of the fluorescently labeled proteins.

*Fluorescence Microscopy*: Fluorescence microscopy was conducted on an LSM 880 (Carl Zeiss, Oberkochen, Germany), using Zen Black for microscopic recording and Zen Blue for picture analysis.

*Python-Based Analysis of Pore Diameter and Lamellae Thickness*: The Python script for determining the pore diameters from previous work[13,34] was extended by code for evaluating the lamellae width.[35] For this purpose, the contours of the pores were first identified in the black and white image in which the holes in the lamellae were closed. The distance between each pixel of each pore contour to the pixels of all other pore contours was iteratively calculated and the minimum distance between all pore combinations was stored. Among these, lamellae widths less than 5 and greater than 20 were filtered out in order to consider only neighboring pores.

*Synthesis and Racemic Reduction of Methylketones*: Synthesis and characterization of NDK **1** was performed as previously described.[30]

*Chiral HPLC Analysis*: An Agilent 1260 series HPLC equipped with a Diode Array Detector and a Lux 3µm Cellulose-1 (150×2.00 mm) chiral column (Phenomenex) was used for chiral analysis. The analysis of biocatalytic NDK reaction products by chiral HPLC was performed as previously described.[28] In brief, the reaction analysis of **1**, the dried ethyl acetate extractions from the crude reaction mixtures were resuspended in 100 µL of the mobile phase (90% n-heptane, 10% 2-propanol) and 10 µL of that solution were injected into the HPLC instrument. The separation was obtained at 10 °C with isocratic elution and a flow rate of 0.5 mL/min. Chromatograms were recorded at 260 nm with the following retention times ($R_t$): Diol: 3.6 min, *syn*-hydroxyketon: 4.9 min, anti-hydroxyketon: 5.3 min, NDK: 7.0 min. To distinguish between the different diol components, a dedicated HPLC method was required, employing a mobile phase of 98% n-heptane and 2% 2-propanol at a flow rate of 1.0 mL $min^{-1}$ and 45 °C. This method has been described in detail previously,[30] where it was also shown that, under the conditions applied there, LbADH exclusively produces the (R,R)-configured diol product.[30]

For the EsPAD decarboxylase activity measurements and flow experiments, HPLC analysis was performed on an Agilent 1260 Infinity II with autosampler and diode array detector as described before with little adjustments.[31] *p*-coumaric acid **4** and 4-vinylphenol **5** were quantified by reverse phase HPLC using a ZORBAX Eclipse XDB C18 column (5 µm, Agilent) with precolumn. The separation was obtained at 30 °C with isocratic elution and a flow rate of 1 mL/min. The mobile phase consisted of 50% acetonitrile and 50% aqueous 0.1% trifluoroacetic acid. Chromatograms were recorded at 260 nm (4-vinylphenol, $R_t$: 3.8 min) and 285 nm (*p*-coumaric acid, $R_t$: 1.8 min).

*Statistical Analysis*: All data was pre-processed using Microsoft Excel and subsequently plotted using Origin Pro showing the mean value with standard deviations which includes at least two independent experiments.

## Supporting Information

Supporting Information is available from the Wiley Online Library or from the author.

## Acknowledgements

This work was supported through the Helmholtz program "Materials Systems Engineering" under the topic "Adaptive and Bioinstructive Materials Systems" (43.33.11). A.J.W. is grateful for support by a Kekulé fellowship by Fonds der Chemischen Industrie (FCI). The authors thank Patrick Bitterwolf for valuable input in the initial phase of this project as well as Julia Weisser and Saskia Gimmel for assistance with protein production, activity and DLS measurements.

Open access funding enabled and organized by Projekt DEAL.

## Conflict of Interest

A related patent was filed including KSR and CMN as inventors.

## Data Availability Statement

The data that support the findings of this study are available from the corresponding author upon reasonable request.

## Keywords

biocatalysis, enzymes, microreactors, non-covalent interactions, porous materials, protein foams

Received: June 2, 2025
Revised: August 12, 2025
Published online:

[1] a) P. J. Nieuwenhuizen, D. Lyon, *J Commer Biotechnol* **2011**, *17*, 159; b) B. Hauer, *ACS Catal.* **2020**, *10*, 8418; c) E. L. Bell, W. Finnigan, S. P. France, A. P. Green, M. A. Hayes, L. J. Hepworth, S. L. Lovelock, H. Niikura, S. Osuna, E. Romero, K. S. Ryan, N. J. Turner, S. L. Flitsch, *Nat. Rev. Methods Primers* **2021**, *1*, 46; d) P. Domínguez de María, *Curr. Opin. Green Sustain. Chem.* **2021**, *31*, 100514; e) A. R. Alcántara, P. Domínguez de María, J. A. Littlechild, M. Schürmann, R. A. Sheldon, R. Wohlgemuth, *ChemSusChem* **2022**, *15*, 202102709; f) R. Buller, S. Lutz, R. J. Kazlauskas, R. Snajdrova, J. C. Moore, U. T. Bornscheuer, *Science* **2023**, *382*, adh8615.

[2] S. Wu, R. Snajdrova, J. C. Moore, K. Baldenius, U. T. Bornscheuer, *Angew. Chem., Int. Ed.* **2021**, *60*, 88.

[3] a) R. A. Sheldon, J. M. Woodley, *Chem. Rev.* **2018**, *118*, 801; b) B. Wiltschi, T. Cernava, A. Dennig, M. Galindo Casas, M. Geier, S. Gruber, M. Haberbauer, P. Heidinger, E. Herrero Acero, R. Kratzer, C. Luley-Goedl, C. A. Müller, J. Pitzer, D. Ribitsch, M. Sauer, K. Schmölzer, W. Schnitzhofer, C. W. Sensen, J. Soh, K. Steiner, C. K. Winkler, M. Winkler, T. Wriessnegger, *Biotechnol. Adv.* **2020**, *38*, 107520; c) A. Usami, *Biosci. Biotechnol. Biochem.* **2025**, *89*, 496.

[4] a) J. M. Sperl, V. Sieber, *ACS Catal.* **2018**, *8*, 2385; b) J. M. Woodley, *Appl. Microbiol. Biotechnol.* **2019**, *103*, 4733; c) J. Nazor, J. Liu, G. Huisman, *Curr. Opin. Biotechnol.* **2021**, *69*, 182.

[5] a) A. Kuchler, M. Yoshimoto, S. Luginbuhl, F. Mavelli, P. Walde, *Nat. Nanotechnol.* **2016**, *11*, 409; b) S. P. France, L. J. Hepworth, N. J. Turner, S. L. Flitsch, *ACS Catal.* **2017**, *7*, 710; c) K. S. Rabe, J. Muller, M. Skoupi, C. M. Niemeyer, *Angew. Chem., Int. Ed.* **2017**, *56*, 13574.

[6] a) G. A. Ellis, W. P. Klein, G. Lasarte-Aragones, M. Thakur, S. A. Walper, I. L. Medintz, *ACS Catal.* **2019**, *9*, 10812; b) P. Du, S. Xu, Z.-K. Xu, Z.-G. Wang, *Adv. Funct. Mater.* **2021**, *31*, 2104819.

[7] S. C. Reddington, M. Howarth, *Curr. Opin. Chem. Biol.* **2015**, *29*, 94.

[8] T. Peschke, P. Bitterwolf, S. Gallus, Y. Hu, C. Oelschlaeger, N. Willenbacher, K. S. Rabe, C. M. Niemeyer, *Angew. Chem., Int. Ed.* **2018**, *57*, 17028.

[9] a) P. Bitterwolf, S. Gallus, T. Peschke, E. Mittmann, C. Oelschlaeger, N. Willenbacher, K. S. Rabe, C. M. Niemeyer, *Chem. Sci.* **2019**, *10*, 9752; b) P. Bitterwolf, F. Ott, K. S. Rabe, C. M. Niemeyer, *Micromachines (Basel)* **2019**, *10*, 783; c) T. Peschke, P. Bitterwolf, K. S. Rabe, C. M. Niemeyer, *Chem Engin Technol* **2019**, *42*, 2009.

[10] E. Mittmann, S. Gallus, P. Bitterwolf, C. Oelschlaeger, N. Willenbacher, C. M. Niemeyer, K. S. Rabe, *Micromachines (Basel)* **2019**, *10*, 795.

[11] T. Peschke, P. Bitterwolf, S. Hansen, J. Gasmi, K. S. Rabe, C. M. Niemeyer, *Catalysts* **2019**, *9*, 164.

[12] P. Bitterwolf, A. E. Zoheir, J. Hertel, S. Kröll, K. S. Rabe, C. M. Niemeyer, *Chem. - Eur. J.* **2022**, *28*, 202202157.

[13] J. S. Hertel, P. Bitterwolf, S. Kröll, A. Winterhalter, A. J. Weber, M. Grösche, L. B. Walkowsky, S. Heißler, M. Schwotzer, C. Wöll, T. van de Kamp, M. Zuber, T. Baumbach, K. S. Rabe, C. M. Niemeyer, *Adv. Mater.* **2023**, *35*, 2303952.

[14] J. E. Dueber, G. C. Wu, G. R. Malmirchegini, T. S. Moon, C. J. Petzold, A. V. Ullal, K. L. Prather, J. D. Keasling, *Nat. Biotechnol.* **2009**, *27*, 753.

[15] V. S. Rao, K. Srinivas, G. N. Sujini, G. N. S. Kumar, *Int. J. Proteom.* **2014**, *2014*, 147648.

[16] a) L. Albertsen, Y. Chen, L. S. Bach, S. Rattleff, J. Maury, S. Brix, J. Nielsen, U. H. Mortensen, *Appl. Environ. Microbiol.* **2011**, *77*, 1033; b) H. Lee, W. C. DeLoache, J. E. Dueber, *Metab. Engin.* **2012**, *14*, 242.

[17] R. A. Rocha, L. Esquirol, V. Rolland, P. Hands, R. E. Speight, C. Scott, *Enzyme Microb.Technol* **2023**, *169*, 110268.

[18] B. Z. Harris, B. J. Hillier, W. A. Lim, *Biochemistry* **2001**, *40*, 5921.

[19] J. E. Dueber, B. J. Yeh, K. Chak, W. A. Lim, *Science* **2003**, *301*, 1904.

[20] a) A. S. Kim, L. T. Kakalis, N. Abdul-Manan, G. A. Liu, M. K. Rosen, *Nature* **2000**, *404*, 151; b) K. E. Prehoda, J. A. Scott, R. D. Mullins, W. A. Lim, *Science* **2000**, *290*, 801.

[21] a) L. Oliveira, A. Cahill, L. Wuscher, K. R. Green, V. Bemmer, B. R. Lichtenstein, *Faraday Discuss.* **2024**, *252*, 468; b) D. T. Monterrey, I. Ayuso-Fernández, I. Oroz-Guinea, E. García-Junceda, *Biotechnol. Adv.* **2022**, *60*, 108016.

[22] D. Chai, J. Boitreaud, J. Dent, M. McPartlon, J. Meier, V. Reis, A. Rogozhnikov, K. Wu, *bioRxiv* **2024**, https://doi.org/10.1101/2024.10.10.615955.

[23] F. Qi, M. Motz, K. Jung, J. Lassak, D. Frishman, *PLoS Comput. Biol.* **2018**, *14*, 1005987.

[24] J. Iwanczyk, D. Damjanovic, J. Kooistra, V. Leong, A. Jomaa, R. Ghirlando, J. Ortega, *J. Bacteriol.* **2007**, *189*, 3176.

[25] H. Park, A. Dovas, D. Cox, in *Encyclopedia of Signaling Molecules*, (Ed: S. Choi), Springer, New York, New York, NY **2012**.

[26] M. P. Meissner, J. M. Woodley, *Nat. Catal.* **2022**, *5*, 2.

[27] D. G. Gibson, L. Young, R. Y. Chuang, J. C. Venter, C. A. Hutchison III, H. O. Smith, *Nat. Methods* **2009**, *6*, 343.

[28] M. Kearse, R. Moir, A. Wilson, S. Stones-Havas, M. Cheung, S. Sturrock, S. Buxton, A. Cooper, S. Markowitz, C. Duran, T. Thierer, B. Ashton, P. Meintjes, A. Drummond, *Bioinformatics* **2012**, *28*, 1647.

[29] T. Peschke, M. Skoupi, T. Burgahn, S. Gallus, I. Ahmed, K. S. Rabe, C. M. Niemeyer, *ACS Catal.* **2017**, *7*, 7866.

[30] M. Skoupi, C. Vaxelaire, C. Strohmann, M. Christmann, C. M. Niemeyer, *Chem. - Eur. J.* **2015**, *21*, 8701.

[31] M. Peng, M. Franzreb, A. J. Weber, P. Lemke, C. M. Niemeyer, K. S. Rabe, *ChemCatChem* **2024**, *16*, 202400092.

[32] F. Ott, K. S. Rabe, C. M. Niemeyer, G. Gygli, *ACS Catal.* **2021**, *11*, 10695.

[33] M. Grosche, A. E. Zoheir, J. Stegmaier, R. Mikut, D. Mager, J. G. Korvink, K. S. Rabe, C. M. Niemeyer, *Small* **2019**, *15*, 1901956.

[34] A. J. Weber, J. S. Hertel, K. S. Rabe, C. M. Niemeyer, Karlsruhe Institute of Technology **2023**, https://doi.org/10.35097/1861.

[35] A. J. Weber, J. S. Hertel, K. S. Rabe, C. M. Niemeyer, Karlsruhe Institute of Technology **2025**, https://doi.org/10.35097/u625jk6q24hvxq21.